SCIENTIFIC REPORTS

OPEN

SUBJECT AREAS:
SENSORS AND BIOSENSORS
NANOPARTICLES

Received
3 June 2014

Accepted
3 September 2014

Published
23 October 2014

Correspondence and requests for materials should be addressed to S.L. (szliu@dicp.ac.cn)

$Ag_x@WO_3$ core-shell nanostructure for LSP enhanced chemical sensors

Lijie Xu[1], Ming-Li Yin[1,3] & Shengzhong (Frank) Liu[1,2]

[1]Key Laboratory of Applied Surface and Colloid Chemistry, Chinese National Ministry of Education; School of Materials Science & Engineering, Shaanxi Normal University, Xi'an 710062, China, [2]Dalian Institute of Chemical Physics, National Laboratory for Clean Energy, Dalian, 116023, China, [3]School of Science, Xi'an Technological University, Xi'an 710032, China.

Exceptional properties of graphene have triggered intensive research on other 2D materials. Surface plasmon is another subject being actively explored for many applications. Herein we report a new class of core-shell nanostructure in which the shell is made of a 2D material for effective plasmonic propagation. We have designed a much enhanced chemical sensor made of plasmonic Ag_x@(2D-WO_3) that combines above advantages. Specifically, the sensor response increases from 38 for Ag_x-WO_3 mixture to 217 for the Ag_x@(2D-WO_3) core-shell structure; response and recovery time are shortened considerably to 2 and 5 seconds; and optimum sensor working temperature is lowered from 370°C to 340°C. Light irradiation is found to increase the Ag_x@(2D-WO_3) sensor response, particularly at blue wavelength where it resonates with the absorption of Ag nanoparticles. Raman scattering shows significantly enhanced intensity for both the 2D-WO_3 shell and surface adsorbates. Both the resonance sensor enhancement and the Raman suggest that the improved sensor performance is due to nanoplasmonic mechanism. It is demonstrated that (1) 2D material can be used as the shell component of a core-shell nanostructure, and (2) surface plasmon can effectively boost sensor performance.

Owing to its unique one-atom thick 2D structure, graphene has shown exceptional characteristics in mechanical, thermal, electronic and optical properties[1,2], demonstrating its potential to revolutionize many applications ranging from teraherz frequency manipulation[3], fuel cells[4], supercapacitors[5], highly sensitive biosensors[6,7], solar cells[8] to various sensor and actuator applications[9]. These intriguing prospects have triggered intensive research on graphene to expand to other 2D materials[2,10] such as isolated monolayer atomic crystals, MoS_2, WS_2, WO_3, WSe_2, other dichalcogenides and layered oxides, hexagonal boron nitride, etc. In fact, it is expected that the research effort will reach the same intensity as that on graphene[2].

There are few limited 2D oxides known so far including mono-layers of TiO_2, MoO_3, WO_3, mica and a few perovskite-like crystals[11,12]. As oxides, they are less susceptible to air but tend to partially lose oxygen at elevated temperature and chemisorb organic compounds. In addition, these monoatomic-layer oxides often have quantum effect enhanced characteristic such as lower dielectric constants, larger bandgap, charge density waves, etc.[13,14], likely leading to much better chemical sensor performance. As strong chemical bonds provide in-plane stability, whereas much weaker van-der-Waals-like forces allow large spacing between layers, 2D crystals provide enough room for gas molecules to enter into the spacing between layers for improved sensor sensitivity. WO_3, a wide bandgap semiconductor with its graphene-like 2D layered structure and good sensor response to a variety of volatile compounds, is a perfect model oxide in this category.

Meanwhile, metal particles with nanometer dimension have shown many unprecedented attributes, such as surface plasmon (SP), light-scattering, catalysis, biologic recognition, etc.[15]. Surface plasmons (SPs) are electromagnetic waves coupled to the collective oscillations of electrons in metal nanoparticles (NPs). Among well-known plasmonic metal elements, including Au, Cu, Al and Li, Ag is considered the most important one for its ability to support SPs across spectrum from 300 to 1200 nm[16,17]. In fact, its enhanced efficiencies have been demonstrated for solar cells, surface-enhanced Raman scattering, fluorescence, plasmonic antennas and circuitry[16].

Consequently, $Ag_x@WO_3$ nanostructure is of particular interest as (1) Ag_x nanoparticle (NP) would form an effective core to provide strong localized surface plasmon (LSP) excited across visible spectrum[16]; (2) LSP can be optimized by adjusting the Ag_x core diameter[18]; (3) WO_3 is an excellent gas sensor material by itself; (4) $Ag_x@WO_3$ is expected to be a good Schottky junction sensor; (5) the well-known layered structure of WO_3 at nanometer thickness may provide quantum effect enhanced sensor performance; and (6) the combined structure

of nano Ag_x core and the layered WO_3 shell could lead to a new generation of quantum effect enhanced gas sensors.

Here we report a new class of core-shell nanostructure (CSNS) in which the shell is made of a 2D layered material for effective LSP propagation. Using the concept, we have designed and fabricated a much enhanced chemical sensor made of plasmonic Ag_x@(2D-WO_3) CSNS – a product combined advantages of both 2D-WO_3 and LSP of Ag nanoparticle (NP). The sensor response increases from 38, for the best sensor based on simple mixture of WO_3 and Ag NPs, to 217 for sensor based on Ag_x@(2D-WO_3); under a weak blue LED irradiation at only 17 mW/cm^2, the $Ag_{(25nm)}$@(2D-WO_3) based sensor response increases further to 408; response and recovery time are shortened considerably to 2 and 5 seconds. Moreover, optimum sensor working temperature is lowered from 370°C to 340°C. It is also found that white light irradiation at ~1 sun intensity increases Ag_x@(2D-WO_3) sensor response by more than 3 times comparing to its dark measurement. Raman scattering of the CSNS shows significantly enhanced intensity for both the 2D-WO_3 shell and ethanol molecules adsorbed on it, suggesting that the enhancement is due to nanoplasmonic mechanism. It shows that 2D material can be used as the shell component of a CSNS, and this may represent a new class of material. Moreover, it also appears that this is the first time for LSP being used to effectively boost chemical sensor performance. It is expected that this may pave a way for different combinations of nano metal core and 2D-semiconductor shell materials and new LSP enhanced nano-devices.

Results

Fabrication of Ag_x@(2D-WO_3) CSNS. Size-controlled Ag NPs with diameter ranging from ~25 nm to ~60 nm, referenced by formula $Ag_{(diameter)}$ as $Ag_{(25nm)}$ and $Ag_{(60nm)}$, were synthesized using a well-developed method[19]. As illustrated in Supplementary Fig. S1a online, the Ag NPs were dispersed into a Na_2WO_4 solution first, upon adding HNO_3, Ag_x@H_2WO_4 precipitate was formed. An extensive high temperature treatment process was then used to remove water from the precipitate to turn it into Ag_x@WO_3 CSNS. For comparison, nano Ag_x-WO_3 mixture was prepared by simply adding preformed WO_3 powder into Ag NP colloid, separating, cleaning, and drying using similar procedures.

X-Ray diffraction of pure WO_3, Ag_x-WO_3 mixture and Ag_x@(2D-WO_3) samples. Figure 1 shows X-ray diffraction (XRD) patterns between 22° ~ 25° of pure WO_3, Ag_x-WO_3 mixture and Ag_x@(2D-WO_3). Both pure WO_3 and Ag_x-WO_3 mixture each have three well defined peaks at 2θ = 23.12°, 23.59° and 24.38°, corresponding to (002), (020) and (200) diffractions of monoclinic crystal structure with d spacing 0.385, 0.377 and 0.365 nm or interlayer spacing 0.77, 0.76 and 0.73 nm respectively. However, the Ag_x@(2D-WO_3) core-shell samples each shows two sets of diffraction peaks: the first set is identical to what observed from the pure WO_3 sample, in addition, each of the three main peaks shows a clearly resolved shoulder peak on its left side, indicating an additional phase with increased interlayer spacing. We attribute the first set to pure WO_3, and the second phase the layered WO_3 in the Ag_x@(2D-WO_3) CSNS. When one side of the WO_3 sheet bonds to the spherical Ag core surface, it distorts the WO_3 structure, leading to the increased interlayer spacing. As the distortion would cause somewhat irregularity, it is expected that FWHM of the XRD peak would be broadened. Indeed, the (200) shoulder peak of the Ag_x@(2D-WO_3) CSNS is widened to FWHM = 0.19 degrees, comparing to FWHM = 0.13 degrees for its main peak.

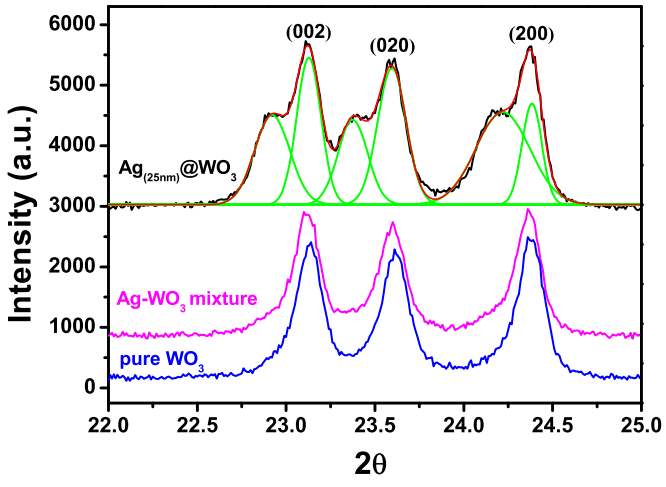

Figure 1 | XRD patterns of the pure WO_3, Ag_x-WO_3 mixture and $Ag_{(25nm)}$@(2D-WO_3).

Microscopic characterization of Ag_x@(2D-WO_3) CSNS. Transmission electron microscopy (TEM) of pure WO_3, Ag_x@(2D-WO_3) and Ag_x-WO_3 mixture samples revealed similar layered WO_3 structure, showing that the WO_3 shell in the Ag_x@(2D-WO_3) CSNS indeed maintains its layered structure around the Ag_x core. More specifically, Fig. 2a is a TEM image of an $Ag_{(60nm)}$@(2D-WO_3) CSNS, both core and shell contours are clearly displayed. For comparison, images of other samples are provided in the Supplementary Fig. S5 online. Probably due to the spherical nature of the Ag_x core structure, the layered WO_3 shell structure was not resolved at the same degree of resolution.

To better resolve the WO_3 shell structure, the $Ag_{(60nm)}$@(2D-WO_3) CSNS sample was cleaned using dilute ammonium solution. TEM image (upper right inset) of the sample shows clearly resolved layered structure. The spacing between adjacent layers is ~0.7–1.2 nm. As it is significantly larger than the layer spacing in the standard monoclinic WO_3 structure[20], we believe that it is related to the secondary phase as observed in the XRD analysis. The lower right inset shows the fringe spacing of 0.37 nm indexed to the (200) planes of monoclinic WO_3.

Figure 2b, c shows selected area electron diffraction (SAED) patterns of the $Ag_{(60nm)}$ core and the WO_3 shell. The former can be indexed to face-centered-cubic crystal structure of Ag NP with symmetry Fm3m. The latter is assigned to the WO_3 monoclinic crystal with symmetry P21/n.

X-ray photoelectron spectroscopy (XPS). The Ag_x@(2D-WO_3) CSNS and simple Ag_x-WO_3 mixture samples were analyzed using XPS. In order to expose fresh Ag from the samples, an ion sputtering process was used to clean them immediately before the XPS analysis. Figure 3 shows the Ag 3d XPS of Ag_x@(2D-WO_3) CSNS and Ag_x-WO_3 mixture. It is clear that while the Ag_x-WO_3 mixture gives the Ag $3d_{5/2}$ and Ag $3d_{3/2}$ peaks at 368.3 eV and 374.3 eV, the peaks of Ag_x@(2D-WO_3) CSNS shifted to 368.0 eV and 374.1 eV, respectively. As free Ag sample has the Ag 3d peaks at 368.3 eV and 374.3 eV[21], no shift is found for the Ag_x-WO_3 mixture. However, there are significant downshifts for the Ag_x@(2D-WO_3) CSNS sample, indicating that there is an effective electron transfer from the WO_3 shell to the Ag core and in other words, the Schottcky junction is formed at the Ag/WO_3 interface in the CSNS, while there is no obvious Schottcky junction in the Ag_x-WO_3 mixture.

Chemical sensor fabrication and analysis. For device fabrication (see Supplementary Fig. S1b online), a proper amount of sample (WO_3, Ag_x-WO_3 mixture, or Ag_x@WO_3) was ground with a few drops of water in a quartz mortar to form slurry[22]. The slurry was then coated onto a ceramic tube equipped with an Au terminal incorporated with two Pt wire leads on each end. A resistive heating wire coil, set in the center of the tube, was employed as a heater to control sensing temperature. Sensor performance was tested on a WS-30A gas sensitivity instrument[23]. The sensor

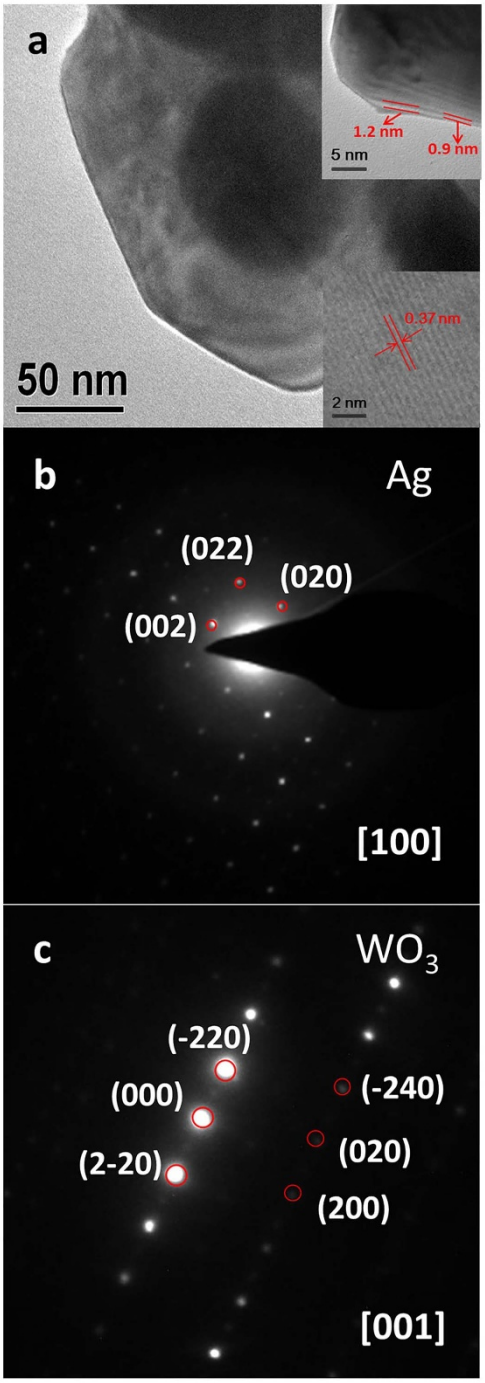

Figure 2 | TEM image and SAED pattern of pure WO_3 and $Ag_{(60nm)}$@(2D-WO_3) CSNS. (a), $Ag_{(60nm)}$@(2D-WO_3) CSNS with the core and the shell clearly resolved. The upper right inset is HRTEM image of $Ag_{(60nm)}$@(2D-WO_3) CSNS showing clearly resolved layered structure, and the lower right inset shows the fringe spacing of 0.37 nm indexed to the (200) planes. (b), SAED pattern of the $Ag_{(60nm)}$ core can be indexed to standard Ag FCC crystal structure. (c), SAED pattern of the WO_3 shell assigned to monoclinic structure.

response (S) is defined as Ra/Rg in reducing gas atmosphere, where Ra and Rg are electrical resistance of the gas sensor in air and in testing gas atmosphere, respectively. For the test, the sensor is heated to desired temperature before Ra is measured in fresh air for 20 seconds. The test vapor is then introduced into the sensor test chamber to measure Rg as a function of time for ~60 seconds. The chamber is then opened to measure resistance until it recovers to the

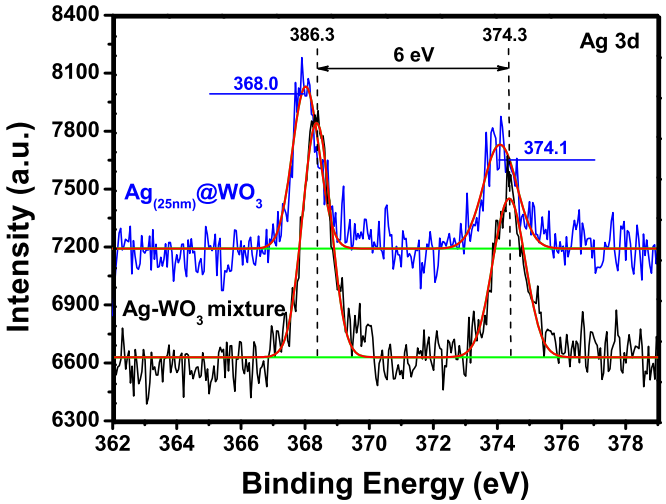

Figure 3 | XPS of Ag 3d spectra in Ag_x@(2D-WO_3) CSNS and the simple Ag_x-WO_3 mixture.

initial value measured in fresh air. The response and recovery time are defined as the time taken by the sensor to achieve 90% of the entire resistance change for target gas adsorption and desorption, respectively (Fig. 4).

Sensor results. The sensor response was measured with varied alcohol vapor concentration at different working temperatures. Figure 4 plots the results including sensor response, as well as response and recovery curves (as insets) for sensors using pure WO_3, Ag_x-WO_3 mixture, $Ag_{(25nm)}$@(2D-WO_3), $Ag_{(35nm)}$@(2D-WO_3), $Ag_{(45nm)}$@(2D-WO_3) and $Ag_{(60nm)}$@(2D-WO_3) towards 100 ppm alcohol vapor. It is clear that sensors made of Ag_x@(2D-WO_3) CSNS show significantly better performance comparing to those from pure WO_3 and Ag_x NP-WO_3 mixture. For two sensors made of pure WO_3 and the Ag_x NP-WO_3 mixture, the optimum sensor working temperature is 370°C. All other sensors based on Ag_x@(2D-WO_3) CSNS show lower optimum working temperature 340°C. Moreover, the first two sensors without core-shell structure have significantly lower responses but longer response and recovery time. Supplementary Table S1 online summarizes key sensor performance parameters. It shows that all key sensor parameters are poorer for sensors based on pure WO_3 and the Ag_x NP-WO_3 mixture, comparing to their core-shell Ag_x@(2D-WO_3) counterparts. More specifically, they have the lowest sensor response (32 and 38 respectively), highest optimum sensor working temperature (370°C), and longest response-recovery time. Apparently, the Ag_x@(2D-WO_3) CSNS improves all key sensor performance parameters. For example, with the CSNS, the optimum working temperature was lowered to 340°C; sensor response time was reduced to 2–4 seconds, and recovery time to 5–7 seconds. The sensor made of $Ag_{(25nm)}$@(2D-WO_3) gives the best overall performance: response increased by ~7 times to 217 comparing to pure WO_3; optimum sensor working temperature lowered to 340°C; and response and recovery time shortened to 2 and 5 seconds.

Sensor response under illumination. We measured sensor response as a function of illumination wavelength using LEDs emitting at 405 nm, 530 nm and 680 nm. For the tests, illumination intensity at the sensor was attenuated to 17 mW/cm^2 for all wavelengths. Figure 5a shows the sensor response of a $Ag_{(25nm)}$@(2D-WO_3) CSNS based sensor at their respective optimum sensor working temperature for 100 ppm alcohol vapor. It shows that when irradiated using a 405 nm blue LED, the sensor response increases by 188% from 217 to 408, while the 530 nm and 680 nm LEDs improve the sensor performance by only ~10%.

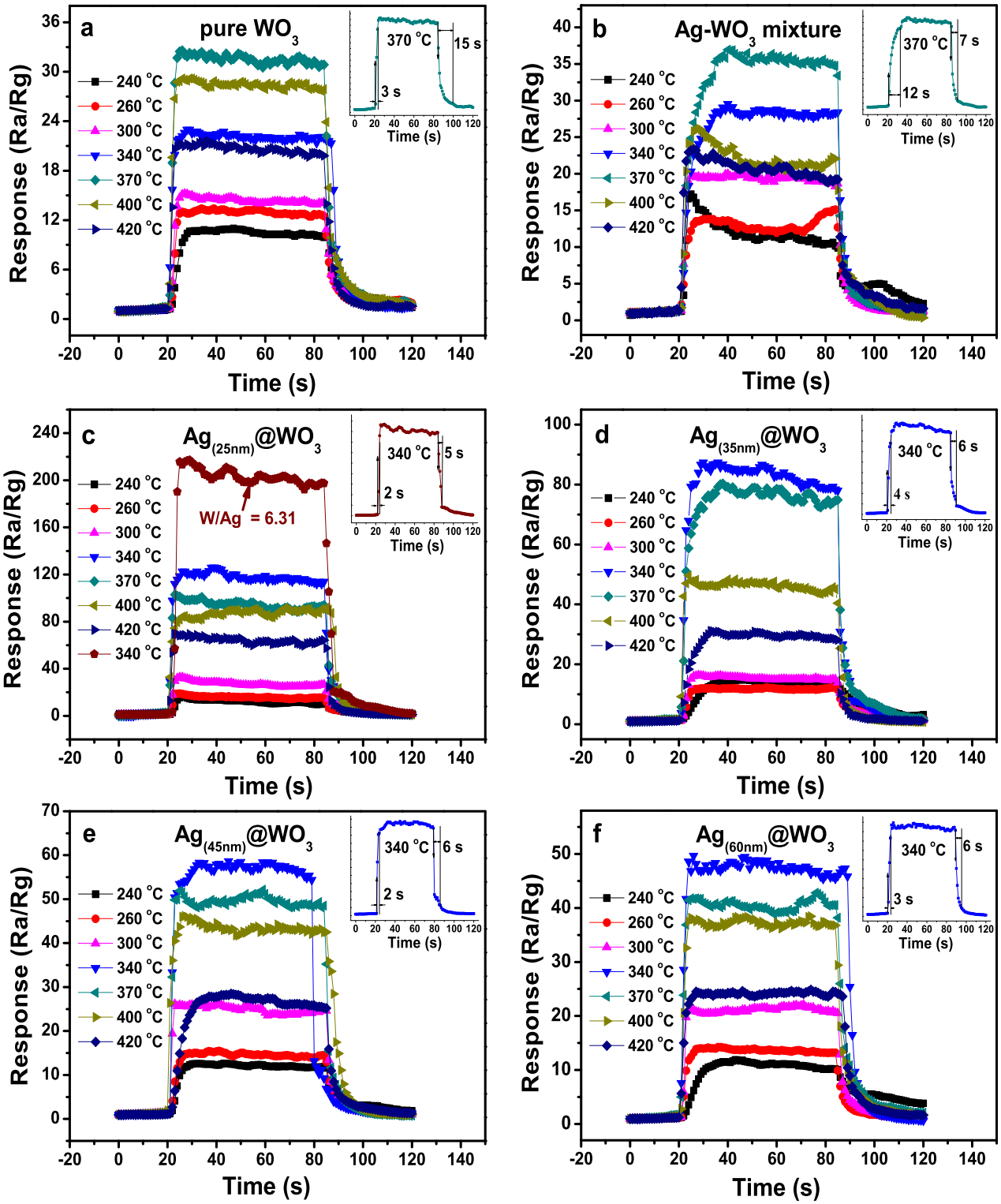

Figure 4 | Transient response at different temperatures for sensors using 100 ppm alcohol vapor exposure. The upper-right inset in each figure shows corresponding response and recovery curves for the senor at its optimum working temperature. (a), pure WO_3; (b), Ag_x-WO_3 mixture; (c), $Ag_{(25nm)}$@(2D-WO_3); (d), $Ag_{(35nm)}$@(2D-WO_3); (e), $Ag_{(45nm)}$@(2D-WO_3); (f), $Ag_{(60nm)}$@(2D-WO_3).

We also measured sensor response as a function of light illumination intensity using a xenon arc light source (150 W) attenuated using neutral density filters. Figure 5b shows normalized response for sensors based on $Ag_{(25nm)}$@(2D-WO_3) CSNS, Ag_x-WO_3 mixture and pure WO_3, measured at their respective optimum sensor working temperature for 100 ppm alcohol vapor under different illumination ranging from darkness to ~1 sun intensity. For comparison, the response of the pure WO_3 sensor measured at darkness is defined as 1 and all others are scaled against it. For sensors based on pure WO_3 and the simple Ag_x-WO_3 mixture, their responses increase linearly with illumination intensity. However, the increases are very limited. When light intensity increases from darkness to 87 mW/cm^2, response of the pure WO_3 sensor increases by only ~40%, and the one with simple Ag_x-WO_3 mixture by ~60%. The

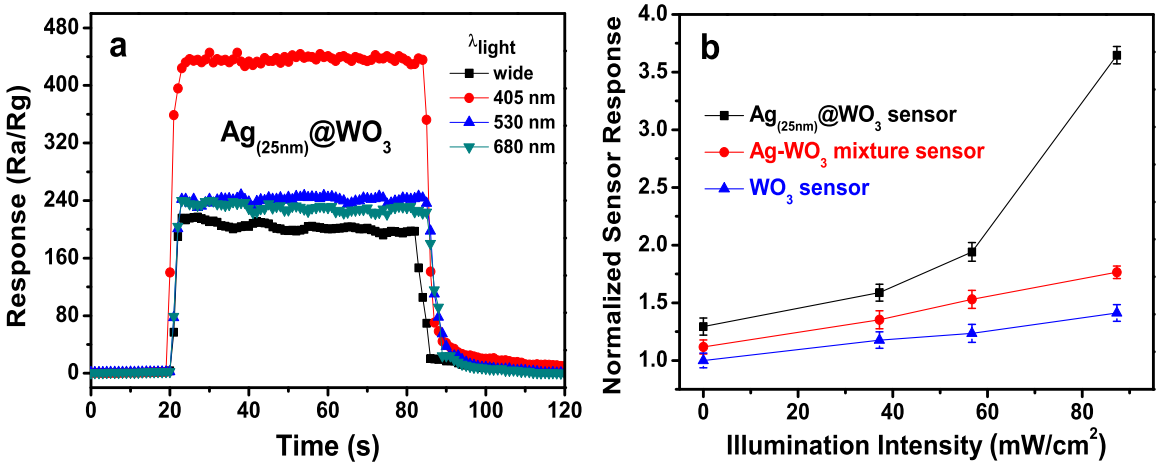

Figure 5 | Sensor response under illumination. (a), Sensor response of $Ag_{(25nm)}$@(2D-WO_3) CSNS at different wavelength of LED irradiation. (b), Normalized sensor response for $Ag_{(25nm)}$@(2D-WO_3) CSNS, Ag_x-WO_3 mixture and pure WO_3 vs. light illumination intensity using a xenon arc light source (150 W) attenuated using neutral density filters. Error bars were determined from fit uncertainty in the corresponding data analysis.

sensor made of $Ag_{(25nm)}$@(2D-WO_3) CSNS shows a much greater dependence on light intensity. When measured at 87 mW/cm^2, response increases by ~308% comparing to its measurement in darkness.

Discussion

It is not surprising to see WO_3 in the Ag_x@(2D-WO_3) CSNS adopted its 2D layered structure. During our preparation, Ag_x@H_2WO_4 was synthesized first; it was then heated at 180°C for 24 hours for it to fully decompose into Ag_x@WO_3. Upon another high temperature heat treatment at 500°C for 2 hours, it is expected that the WO_3 shell would relax to its most stable 2D layered structure, allowing its inner peripheral to bond to the Ag_x core.

It is known that oxygen vacancies in WO_3 lattice structure act as electron donors to provide electrons to its conduction band, making WO_3 an n-type semiconductor[24] and the Ag/WO_3 interface a Schottky junction, as illustrated in Supplementary Fig. S3 online. As the work function of n-type WO_3 is smaller than that of Ag, electrons transfer from WO_3 to Ag in the Ag_x@(2D-WO_3) CSNS, resulting in an interfacial dipole layer[25]. The electrically polarized potential at the interface further lowers work function of Ag, and thus decreases barrier height[25], leading to negatively charged Ag surface and positively charged WO_3 surface or depletion zone. When the Ag_x@(2D-WO_3) CSNS is exposed to air, it absorbs oxygen and produces negatively charged oxygen species such as $O^{\delta-}$, $O_2^{\delta-}$, etc. on its surface. As more electrons are depleted by absorbed oxygen species, the electrical resistance of the sensor (Ra) is effectively increased. On the contrary, when it is exposed to reducing atmosphere like alcohol vapor, the electron depleted WO_3 surface gains electrons from the alcohol molecules, resulting in reduced electrical resistance (Rg) and therefore enlarged (Ra/Rg), leading to enhanced chemical sensor response (S = Ra/Rg).

Supplementary Fig. S4 online shows an energy band diagram for the Schottky junction formed in the Ag_x@(2D-WO_3) CSNS. The negative XPS peak shifts for Ag 3d is caused by the electron transfer from WO_3 to Ag, forming wider electron depletion layer when the sensor is exposed to air, leading to higher sensor resistance Ra. When the sensor is exposed to reducing gas such as ethanol, electrons return to WO_3 conduction band due to the electron transfer between surface oxygen species and the reducing gas, resulting in reduced barrier height (Φ_B) and sensor resistance Rg. The combination of higher Ra and lower Rg would yield better gas sensor response as it is defined as S = Ra/Rg.

Ag NPs act as nano antennas when they are excited by electromagnetic radiation[16]. In present case, our preparation process for the Ag_x@(2D-WO_3) CSNS warrants an intimate connection between the WO_3 shell and the Ag_x NP core. The Ag_x@(2D-WO_3) based sensors indeed give surprisingly higher responses. We attribute the improvements to the unique combination of surface plasmonic effect of the Ag_x NP core, the 2D layered structure of the WO_3 shell, and a high quality Ag_x/(2D-WO_3) interface. Behaving like nano antennas, Ag NPs receive excitation energy from electromagnetic radiation and transfer it via the Ag_x/WO_3 Schottky junction to the WO_3 surface, leading to collective oscillation of electron density[26,27]. These oscillations, known as LSPs, then lead to narrow regions of enhanced electromagnetic field strength[27] and consequently improved sensor responses. The LSPs enhanced field strength in Ag_x NP core therefore effectively extends to the shell surface, and the shell in fact behaves as an extension of LSPs from the core, leading to the changed E-field on the WO_3 shell surface.

In case of Ag_x NP-WO_3 mixture, both WO_3 powder and Ag_x NPs were preformed separately before being mixed together. On one hand, their surfaces were saturated already by different chemical species during their syntheses. On the other hand, there must be contaminant remains in between the Ag_x and WO_3 particles. Therefore, the spacing between Ag_x NP and WO_3 particles are too large for effective junction formation and LSP propagation. Consequently, there is no significant improvement in sensor performance for the Ag_x NP-WO_3 mixture.

It is also shown in Fig. 4 that within the group of Ag_x@(2D-WO_3) based sensors, when the Ag_x core diameter was reduced from 60 nm to 25 nm, the smaller the Ag_x core diameter, the better the sensor performance. The smallest Ag_x core with 25 nm diameter gives the best overall performance, including highest sensor response, sharpest response and recovery time and lowest optimum sensor working temperature. This trend is anticipated considering that the ionization potential (IP) of Ag NP is expected to increase when it gets smaller due to its gradually increased electron affinity (EA). In fact, IP of Ag clusters or NPs has been studied in great detail[28,29]. The detailed model calculations of electronic/geometric structure exist for s^1-electron metal cluster neutrals and ions in various size ranges. These calculations are found to be accurate enough for interpretation of optical response measurements on Ag_x[30] as well as other metals[31]. The IPs for clusters follow the equation (1) moderately well[30]. Here *WF* is the crystalline metal work function; *R* the sphere radius equivalent to the volume of an x-atom metal cluster[29]; *a* the element specific extent of (cluster radius independent) electron spillout.

$$WF = IP - (1/2)e^2/(R+a) \quad (1)$$

As EA follows the same trend as IP, when Ag NPs get smaller, both EA and IP increase and the smallest Ag NPs should have highest EA and IP. Therefore in our case, smaller Ag NPs with higher EA capture more electrons from the WO_3 shell, leading to more positive space charge region on the WO_3 shell surface and broadened electron depletion layer, leading to higher sensor response.

Illumination is another key factor for plasmonics. It is expected that higher illumination intensity would result in stronger LSP, leading to better sensor response. However, in order for illumination to take effect, there has to be an effective electron transfer channel between the Ag_x core and the WO_3 shell structure.

For sensors based on pure WO_3 and the simple Ag_x-WO_3 mixture, even though their responses do increase with illumination intensity, the increased magnitudes are very limited. When light intensity increases from darkness to 87 mW/cm^2, response of the pure WO_3 sensor increases by only ~40%, and the one with simple Ag_x-WO_3 mixture by ~60%. The sensor made of $Ag_{(25nm)}$@(2D-WO_3) CSNS shows a much greater increase. When measured at 87 mW/cm^2, response boosts by ~308% comparing to its measurement in darkness, revealing that there is an intimate junction between the Ag_x core and the 2D-WO_3 shell. As for the sensor irradiated under different wavelength of LEDs, when irradiated at 405 nm, the sensor response increases by 188% (from 217 to 408). When illuminated at 530 nm and 680 nm, responses increase by only ~10%.

It is well known that Ag nanoparticles can support surface plasmons. As the resonance wavelength for the $Ag_{(25nm)}$ is measured at ~404 nm (see Supplementary Fig. S2 online), it is expected that the sensor response would be increased significantly at 405 nm. As the sensor response does not change much at other wavelengths, it is clear that the sensor enhancement is due to the surface plasmonic effect.

For semiconductor oxide sensors, it has been a well-known phenomenon that sensor response increases under light illumination[32,33], as it is observed for the pure WO_3 case. However, the increase observed for the $Ag_{(25nm)}$@(2D-WO_3) CSNS sensor is dramatic, suggesting that the increase is caused by the LSP effect of the Ag NP core and the enhanced E-field is effectively propagated to the 2D-WO_3 shell.

To further prove the above interpretation, we conducted a Raman study to see if Ag NP can indeed effectively enhance Raman signal of the WO_3 shell and surface adsorbed alcohol vapor molecules. Figure 6 shows Raman spectra of pure WO_3, Ag_x-WO_3 mixture and Ag_x@(2D-WO_3). It is clear that each has four well-resolved peaks at 272, 326, 717 and 807 cm^{-1}. Peaks centered at 717 and 807 cm^{-1} are attributed to W-O-W stretching vibration mode, and two lower peaks at 272 and 326 cm^{-1} are induced by W-O-W bending mode vibration [(O-W-O)][34]. Comparing to pure WO_3, Ag_x-WO_3 mixture shows slightly enhanced Raman intensity by only ~35%. However, Ag_x@(2D-WO_3) CSNS shows Raman intensity enhanced by as much as 20 times, consistent with what observed from the sensor performance and further proving that LSP is a major factor for the enhanced sensor response.

In conclusion, we developed a new class of CSNS material in which 2D-WO_3 was used as the shell component. We designed and fabricated a LSP enhanced chemical sensor based on Ag_x@(2D-WO_3) CSNS. It is far more effective than sensors made of simple mixture of Ag NP and WO_3 powder. It shows that the unique combination of the Ag core and the 2D layered structure of WO_3 shell results in effective LSP generation and propagation, leading to much enhanced sensor performance. It is expected that more combinations of different metal core and 2D-semiconductor shell will lead to new LSP enhanced nano-devices.

Methods

Fabrication of Ag_x@(2D-WO_3) CSNS. Size-controlled Ag NPs were synthesized using a well-developed method[19]. We have tested Ag NPs with diameter ranging from ~25 nm to ~60 nm, referenced by formula $Ag_{(diameter)}$ as $Ag_{(25nm)}$ and $Ag_{(60nm)}$.

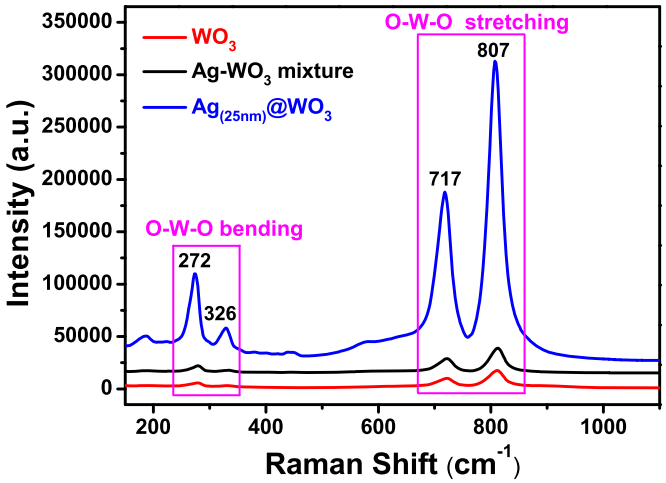

Figure 6 | Raman spectra of pure WO_3, Ag_x-WO_3 mixture, $Ag_{(25nm)}$@(2D-WO_3) measured using 532 nm excitation.

UV-Visible absorbance spectrum (see Supplementary Fig. S2 online) shows a distinct peak with center position red-shifted as Ag diameter increases. More specifically, the peaks are centered at 404 to 412, 425, and 433 nm for $Ag_{(25nm)}$, $Ag_{(35nm)}$, $Ag_{(45nm)}$ and $Ag_{(60nm)}$, respectively[35]. Supplementary Fig. S6 online plots the UV-Visible peak position as a function of the Ag NP diameter. Using the "Haiss equation[36]" and the measured λ_{spr}, the calculated diameter values agree well with measurements. As illustrated in Supplementary Fig. S1a online, the Ag_x@WO_3 CSNS was fabricated as follows: 0.5 g $Na_2WO_4{\cdot}2H_2O$ was first dissolved in 10 ml ultrapure water to prepare Na_2WO_4 solution. Under constant ultrasonication, 50 ml preformed Ag colloid NPs were added into the Na_2WO_4 solution. Note that unless specifically notified, Ag colloid concentration was adjusted to keep final atomic ratio at W/Ag = 30. Subsequently, 5 ml 5 M nitric acid was added in drop by drop under vigorous agitation. The brown suspension was turned into yellow color as H_2WO_4 coated onto the Ag NPs, forming Ag_x@H_2WO_4 precipitate. The mixture was then transferred into a Teflon-lined autoclave, maintained at 180°C for 24 hours. Upon cooling to room temperature, a fine yellow powder product was collected by centrifugal separation; washed using ultrapure water; dried and finally heat treated at 500°C for 2 hours. For comparison, nano Ag_x-WO_3 mixture was prepared by simply adding preformed WO_3 powder into Ag NP colloid, separating, cleaning, and drying using similar procedures.

Characterization. XRD Crystal structure was characterized using a DX-2700 X-ray diffractometer (XRD) using Cu $K_\alpha$radiation (λ = 0.15418 nm). The dimension and morphology of the Ag NPs were characterized using a Nova Nano SEM 450 operated at 1 kV. An UV-Vis spectroscopy (Lambda-950 spectrometer, Perkin Elmer, USA) was used to measure the absorbance spectra of Ag NPs. Elemental analysis was performed on an AXIS ULTRA X-ray photoelectron spectroscopy (XPS) instrument using monochromatic Al Kα X-ray source. TEM and SAED were taken using a JEM-2100 TEM. Raman spectroscopy study was conducted on an ALMEGA Dispersive Raman spectrometer with an Ar^+ laser excitation at 514 nm. Gas sensing tests were performed using a WS-30A gas sensitivity instrument (Wei Sheng Electronics Co. Ltd., China) with a test chamber of 30 L (315 mm × 315 mm × 350 mm) in volume.

1. Bonaccorso, F., Sun, Z., Hasan, T. & Ferrari, A. C. Graphene photonics and optoelectronics. *Nature Photon.* **4**, 611–622 (2010).
2. Geim, A. K. & Grigorieva, I. V. Van der Waals heterostructures. *Nature* **499**, 419–425 (2013).
3. Tassin, P. Graphene for terahertz applications. *Science* **341**, 620–621 (2013).
4. Qu, L., Liu, Y., Baek, J. B. & Dai, L. Nitrogen-doped graphene as efficient metal-free electrocatalyst for oxygen reduction in fuel cells. *ACS Nano* **4**, 1321–1326 (2010).
5. Yu, D. & Dai, L. Self-assembled graphene/carbon nanotube hybrid films for supercapacitors. *J. Phys. Chem. Lett.* **1**, 467–470 (2010).
6. Dong, H. *et al.* Highly sensitive multiple microRNA detection based on fluorescence quenching of graphene oxide and isothermal strand-displacement polymerase reaction. *Anal. Chem.* **84**, 4587–4593 (2012).
7. Liu, Y., Yu, D., Zeng, C., Miao, Z. & Dai, L. Biocompatible graphene oxide-based glucose biosensors. *Langmuir* **26**, 6158–6160 (2010).
8. Yu, D., Park, K., Durstock, M. & Dai, L. Fullerene-grafted graphene for efficient bulk heterojunction polymer photovoltaic devices. *J. Phys. Chem. Lett.* **2**, 1113–1118 (2011).
9. Xie, X. *et al.* An asymmetrically surface-modified graphene film electrochemical actuator. *ACS Nano* **4**, 6050–6054 (2010).
10. Fuhrer, M. S. & Hone, J. Measurement of mobility in dual-gated MoS_2 transistors. *Nature Nanotech.* **8**, 146–147 (2013).

11. Xu, M., Liang, T., Shi, M. & Chen, H. Graphene-like two-dimensional materials. *Chem. Rev.* **113**, 3766–3798 (2013).
12. Butler, S. Z. *et al*. Progress, challenges, and opportunities in two-dimensional materials beyond graphene. *ACS Nano* **7**, 2898–2926 (2013).
13. Novoselov, K. S. *et al*. Two-dimensional atomic crystals. *Proc. Natl. Acad. Sci. USA* **102**, 10451–10453 (2005).
14. Osada, M. & Sasaki, T. Two-dimensional dielectric nanosheets: novel nanoelectronics from nanocrystal building blocks. *Adv. Mater.* **24**, 210–228 (2012).
15. Das, S. K. & Marsili, E. *Nanomaterials-Bioinspired Metal Nanoparticle: Synthesis, Properties and Application* (In Tech, 2011).
16. Rycenga, M. *et al*. Controlling the synthesis and assembly of silver nanostructures for plasmonic applications. *Chem. Rev.* **111**, 3669–3712 (2011).
17. Mubeen, S. *et al*. An autonomous photosynthetic device in which all charge carriers derive from surface plasmons. *Nature Nanotech.* **8**, 247–251 (2013).
18. Lal, S. *et al*. Tailoring plasmonic substrates for surface enhanced spectroscopies. *Chem. Soc. Rev.* **37**, 898–911 (2008).
19. Lee, P. C. & Meisel, D. Adsorption and surface-enhanced Raman of dyes on silver and gold sols. *J. Phys. Chem.* **86**, 3391–3395 (1982).
20. Liang, L. *et al*. High-performance flexible electrochromic device based on facile semiconductor-to-metal transition realized by $WO_3{\cdot}2H_2O$ ultrathin nanosheets. *Sci. Rep.* **3**, 1936; DOI: 10.1038/srep01936 (2013).
21. Moulder, J. F., Stickle, W. F., Sobol, P. E. & Bomben, K. D. *Handbook of X-ray Photoelectron Spectroscopy*, Chastain, J., Ed., (Perkin Elmer Corporation, Eden Prairie, 1992).
22. Yin, M., Liu, M. & Liu, S. Development of an alcohol sensor based on ZnO nanorods synthesized using a scalable solvothermal method. *Sensor Actuat. B-Chem.* **185**, 735–742 (2013).
23. Yin, M., Liu, M. & Liu, S. Diameter regulated ZnO nanorod synthesis and its application in gas sensor optimization. *J. Alloys Compd.* **586**, 436–440 (2014).
24. Gao, X. *et al*. Hydrothermal synthesis of WO_3 nanoplates as highly sensitive cyclohexene sensor and high-efficiency MB photocatalyst. *Sensor Actuat. B-Chem.* **181**, 537–543 (2013).
25. Potje-Kamloth, K. Semiconductor junction gas sensors. *Chem. Rev.* **108**, 367–399 (2008).
26. Anker, J. N. *et al*. Biosensing with plasmonic nanosensors. *Nature Mater.* **7**, 442–453 (2008).
27. Anema, J. R., Li, J. F., Yang, Z. L., Ren, B. & Tian, Z. Q. Shell-isolated nanoparticle-enhanced Raman spectroscopy: expanding the versatility of surface-enhanced Raman scattering. *Annu. Rev. Anal. Chem.* **4**, 129–150 (2011).
28. Alameddin, G., Hunter, J., Cameron, D. & Kappes, M. M. Electronic and geometric structure in silver clusters. *Chem. Phys. Lett.* **192**, 122–128 (1992).
29. Seidl, M., Meiwes-Broer, K. H. & Brack, M. Finitesize effects in ionization potentials and electron affinities of metal clusters. *J. Chem. Phys.* **95**, 1295–1303 (1991).
30. Rothlisberger, V. & Andreoni, W. Structural and electronic properties of sodium microclusters (n = 2–20) at low and high temperatures: new insights from *ab* initio molecular dynamics studies. *J. Chem. Phys.* **94**, 8129–8151 (1991).
31. Rivas, L., Sanchez-Cortes, S., Garcia-Ramos, J. V. & Morcillo, G. Mixed Silver/Gold colloids: a study of their formation, morphology, and surface-enhanced raman activity. *Langmuir* **16**, 9722–9728 (2000).
32. Giberti, A., Malagù, C. & Guidi, V. WO_3 sensing properties enhanced by UV illumination: an evidence of surface effect. *Sensor Actuat. B-Chem.* **165**, 59–61 (2012).
33. Zhang, C. *et al*. Room temperature responses of visible-light illuminated WO_3 sensors to NO_2 in sub-ppm range. *Sensor Actuat. B-Chem.* **181**, 395–401 (2013).
34. Su, C. Y., Lin, H. C. & Lin, C. K. Fabrication and optical properties of Ti-doped $W_{18}O_{49}$ nanorods using a modified plasma-arc gas-condensation technique. *J. Vac. Sci. Technol. B* **27**, 2170–2174 (2009).
35. Li, L. *et al*. Controllable synthesis of monodispersed silver nanoparticles as standards for quantitative assessment of their cytotoxicity. *Biomaterials* **33**, 1714–1721 (2012).
36. Pandikumar, A. & Ramaraj, R. Photocatalytic reduction of hexavalent chromium at gold nanoparticles modified titania nanotubes. *Mater. Chem. Phys.* **141**, 629–635 (2013).

Acknowledgments

We acknowledge financial support from Chinese National University Research Fund (GK261001009), Shaanxi Normal University, Xi'an, China and China Postdoctoral Science Foundation (No.2013M542324).

Author contributions

L.X. conducted all experimental work. L.X. and S.L. wrote the main manuscript text and M.Y. helped in interpretation of XPS, SAED data, etc. All authors reviewed the manuscript.

Additional information

Supplementary information accompanies this paper at http://www.nature.com/scientificreports

Competing financial interests: The authors declare no competing financial interests.

How to cite this article: Xu, L., Yin, M.-L. & Liu, S. $Ag_x@WO_3$ core-shell nanostructure for LSP enhanced chemical sensors. *Sci. Rep.* **4**, 6745; DOI:10.1038/srep06745 (2014).